

Massimo De Vittorio  
Luigi Martiradonna  
John Assad *Editors*

# Nanotechnology and Neuroscience: Nano- electronic, Photonic and Mechanical Neuronal Interfacing

 Springer

# Chapter 3

## In-Cell Recording and Stimulation by Engulfment Mechanisms

Aviad Hai

**Abstract** Neuroscientists have long been using microelectrodes to record and stimulate neural activity—both in vitro and in vivo. On one end of the spectrum of electrode-based techniques are the sharp-glass and patch micropipette electrodes; on the other end are dense arrays of metal-based microelectrodes. Glass micropipette electrodes enable *intracellular* recording of action potentials and synaptic potentials with excellent signal-to-noise ratio, but because of their bulkiness, they allow for the recording and stimulation of only several neurons at a time. In addition, the injury inflicted on the cell plasma membrane during electrode entry and recording limits the duration of the recording session, usually to a small number of hours at most. By contrast, multielectrode devices are able to record and stimulate much larger populations of neurons for durations of weeks and even months. This is made possible due to fabrication technologies that allow for a scalable design of hundreds or even thousands of electrodes. These devices, however, have been able to provide only *extracellular* recording and stimulation with limited signal-to-noise ratio due to the extracellular positioning of the electrode in respect to the neuron’s plasma membrane. The inability to record intracellular signals from many neurons and for long periods of time has thus far prevented neuroscience from answering the most basic and interesting questions regarding learning and memory in large populations of neurons. This is because the vast majority of neurons in complex nervous systems are usually “silent” and will generate an action potential only when their complex synaptic inputs integrate appropriately. We are therefore blind to the rich milieu of synaptic interactions, synaptic plasticity, and subthreshold network oscillations that reflect the state of the studied nervous system. This chapter describes a recently developed technique termed *in-cell recording*. This technique yielded for

---

A. Hai, Ph.D. (✉)

The Hebrew University of Jerusalem, Jerusalem, Israel

Massachusetts Institute of Technology, Cambridge, MA 02139, USA

e-mail: aviadh@MIT.EDU

the first time simultaneous, multisite, long-term recordings of action potentials and subthreshold synaptic potentials with matching quality and signal-to-noise ratio of conventional intracellular glass electrodes and the scalability of fabricated multi-electrode devices. The in-cell recording and stimulation technique makes use of an array of cell-noninvasive micrometer-size protruding gold mushroom-shaped microelectrodes (gM $\mu$ Es). The key to the multielectrode in-cell recording approach is the outcome of three converging cell-biological principles: (a) the activation of endocytotic-like mechanisms in which the cultured cells are induced to actively engulf gM $\mu$ Es that protrude from the substrate, (b) the generation of high seal resistance between the cell's membrane and the engulfed gM $\mu$ E, and (c) the localization of ionic channels (ohmic conductance) in the plasma membrane that faces the gM $\mu$ E. We will describe the electrical, ultrastructural, and cell-biological properties of the interface between the cells and the gM $\mu$ Es and provide the reader with a digest of the published studies carried out for the development of this technique.

### 3.1 Introduction

The emergence of modern neuroscience began when it was first realized that neurons communicate by generating electrical signals that can be amplified and monitored [1–5]. Understanding the physical, chemical, and biological mechanisms that underlie the generation of the electrical signals, their propagation along axons and dendrites, and transmission between neurons (synaptic transmission) greatly depended on the development of appropriate methods to monitor and generate the electrical activities of neurons. The timeline traverses from initial studies of impulse propagation and generation by extracellular electrodes [6, 7] to studies of membrane biophysics, impulse propagation, and synaptic transmission with sharp intracellular glass microelectrodes [5, 8–10] and to studies of membrane properties, synaptic transmission, and single ion channels by the patch clamp technique [11]. As the field progressed, it was clear that further advancement in the understanding of brain functions would require the simultaneous gathering of functional (electrical) information from large populations of neurons for long periods of time (from hours to days and weeks). As aforementioned, the use of sharp or patch microelectrodes for parallel recording or stimulation from large populations of neurons is technically limited as the micromanipulation of the electrode tips toward target cells requires the use of rather bulky micromanipulators [12, 13]. In addition, the duration of intracellular recording and stimulation sessions by sharp-glass and patch electrodes is limited, because, with time, mechanical instabilities damage the plasma membrane or—in the case of the patch electrodes—perfusion of the cytoplasm into the volume of the glass electrode alters the intracellular composition of the cells [11]. These shortcomings precluded effective analysis of the electrical activity of large neural networks.

A solution to these problems was the impressive development of different forms of imaging technologies ranging from the use of voltage-sensitive dyes [14–16] to multiphoton imaging of activity-related calcium concentration transients [17–19]

and to fMRI [20, 21]. The major advantage of these imaging approaches is that they mostly do not harm the cells and can be performed for long periods of time. However, at high enough concentrations, optical imaging agents can be toxic to the cells and also change their phenotype. In addition, most optical neural recording methods require exposure of the tissue to acquire a signal, which falls significantly in deeper planes. It is worth noting that light-based *in vivo* recording and stimulation of neuronal populations has also recently evolved as a strong field of research by the use of optogenetic techniques [22–25] but currently serves mainly as a population-specific stimulation method, with limited novel complementary methodologies to concurrently record neuronal activity by either microfiber optic probes [26] or optical–electrical hybrid arrays [27, 28]. In the case of using fMRI for the recording of neural activity, the temporal resolution is not sufficient, reaching orders of magnitude below that of single action and synaptic potentials. In addition, fMRI suffers from low spatial resolution and the acquired signal reflects indirect manifestations of neuronal electrical activity such as blood flow in capillaries [29].

Concurrently, large arrays of extracellular metal microelectrodes (MEAs) or semiconductor-based micro- and nano-transistors were developed [30–37]. The use of noninvasive extracellular microelectrode arrays enables to record and stimulate large populations of excitable cells for days and months without inflicting mechanical damages to the cell plasma membrane. The method has a time resolution suitable for the acquisition of spikes and synaptic potentials and allows for the stimulation of single neurons using current or voltage pulses [38–40]. The most severe disadvantage of extracellular recording electrodes is their low signal-to-noise ratio and the ambiguity in defining the origin of the recorded signals. Therefore, the use of extracellular electrodes is limited to recordings of field potentials generated by action potentials [41, 42]. Only in rare cases such as the Schaffer collaterals-pyramidal cells synapses in the CA1 region of the hippocampus can synchronized synaptic potentials in highly ordered neuronal networks be picked up by extracellular electrodes [43]. Single excitatory or inhibitory subthreshold synaptic potentials or membrane oscillations cannot be detected by currently used extracellular electrodes technology [44]. These shortcomings limit the use of extracellular recordings to the analysis of spike patterns and frequencies which relies heavily on spike sorting for the determination of the number of neurons which act as sources of the recorded signals [45, 46].

An ideal multiunit recording system should provide a readout that covers the entire spectrum of membrane potential events from the individually recorded neurons. This includes action potentials (APs), subthreshold excitatory and inhibitory postsynaptic potentials (EPSPs and IPSPs, respectively), and subthreshold membrane oscillations. In addition, it should be possible to modulate the activity of individual neurons within the network by the application of current. The system should provide this readout simultaneously from hundreds of individual neurons and with a stable contact with the neurons for days and weeks.

The in-cell recording and stimulation system described herein [47–52] (Fig. 3.1) makes use of an array of cell-noninvasive micrometer-size protruding gold mushroom-shaped microelectrodes (gM $\mu$ Es). The gM $\mu$ E's geometry and chemical functionalization trigger the activation of endocytotic mechanisms in which the

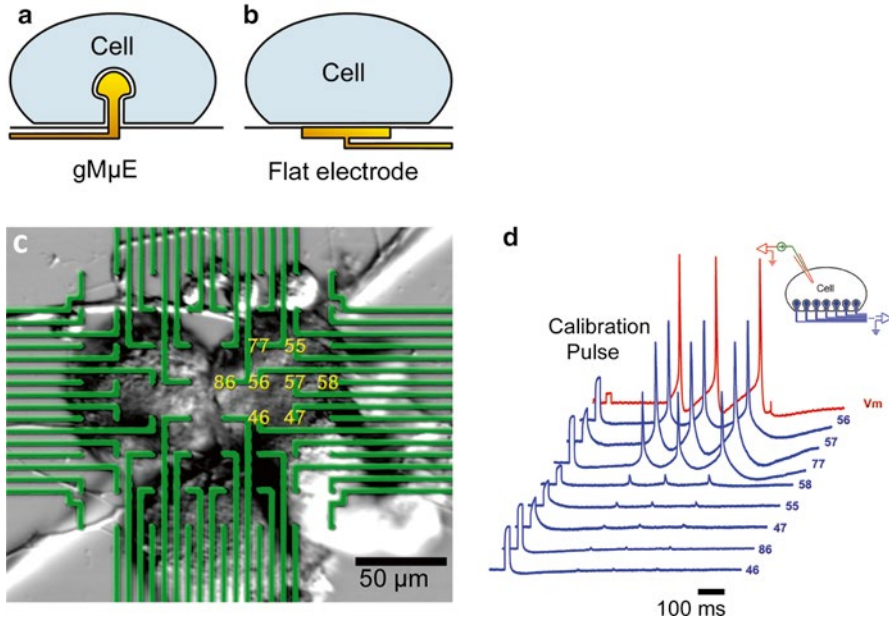


**Fig. 3.1** The in-cell recording configuration. (a) Schematic representation of a neuron engulfing a gold mushroom-shaped microelectrode (gMμE). (b) The geometrical relationships between a neuron and a flat electrode. (c) Three *Aplysia* neurons cultured on an array of 62 gMμEs. (d) Raw action potential recordings from eight gMμEs (indicated by numbers also in c) in response to intracellular stimulation of the neuron by a conventional sharp microelectrode ( $V_m$ ). Each trace depicts initially a 5 mV, 20 ms calibration pulse and then (following a delay) three action potentials. Reproduced from [51] © The Author(s)

cultured cells are induced to actively engulf the gMμEs protruding from the substrate. These processes generate a high seal resistance ( $R_{seal}$ ) between the cell's membrane and the engulfed gMμE and also results in increased ohmic conductance, in the form of either voltage-independent ionic channels or membrane pores in the plasma membrane that faces the gMμE.

We begin with a brief technical description of gMμE fabrication and chemical functionalization followed by ultrastructural studies of the cell–gMμE junction. We then examine cytoskeletal and other cell-biological interactions between neurons and gMμEs and finally demonstrate the resulting high electrical coupling that enables long-term stimulation and recording of action potentials and synaptic potentials from multiple cells with signal-to-noise ratio comparable to that of glass-based micropipette electrodes.

### 3.2 Device Preparation

This section describes some of the technical aspects of device preparation for in-cell recording and stimulation as detailed also in published studies [48–52].

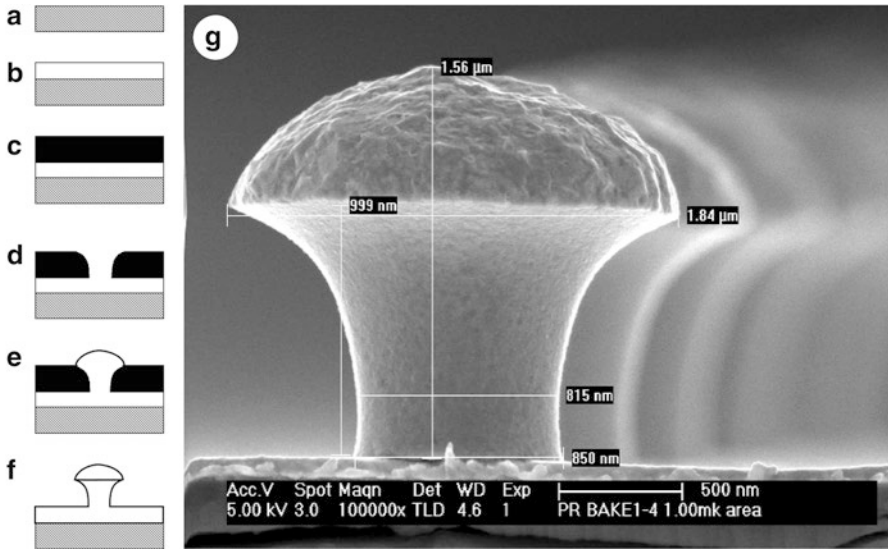


**Fig. 3.2** Fabrication process of gM $\mu$ Es. Silicon or glass samples (a) are coated with a Ti/Au layer (b) by electron-beam evaporation and are then spin-coated with photoresist material (c). Samples undergo photolithography using a photomask to define conducting lines and open holes through the photoresist (d). The gM $\mu$ Es are grown on the surface by way of gold electroplating (e) and the photoresist layer is removed (f). (g) Scanning electron microscopic image of gM $\mu$ Es fabricated on a glass surface. Reproduced from [48] © The Author(s)

### 3.2.1 gM $\mu$ E Fabrication

Device fabrication is based on complementary metal–oxide–semiconductor (CMOS) technology. Arrays of gM $\mu$ E electrodes are prepared on either glass or silicon wafers (Fig. 3.2 and see also refs. [48–52]). The wafers are first dehydrated at 120 °C for 30 min and are then coated with a Ti (10–15 nm)/Au (45–65 nm) layer by way of evaporation (Fig. 3.2b), spin-coated with photoresist S-1813 (4,000 RPM) and baked for 30 min at 90 °C (Fig. 3.2c). The first photolithographic process is performed followed by Au/Ti wet etch to define the leads of the microelectrode array (Karl Suss MJB UV400 mask aligner was used at  $W = 44 \text{ mW cm}^{-2}$  and exposure time of 4.4–4.6 s). Next, a second photolithographic step with thick photoresist is performed to open holes for the deposition of the gM $\mu$ E stalks as well as the contact pads (Fig. 3.2d). Gold mushrooms (along with thick metal on the contact pads) are grown by way of electroplating (Fig. 3.2e). The dimensions and shape of the fabricated gold mushroom roughly imitate the shape of naturally occurring dendritic spines [53], with a stem height of approximately 1  $\mu\text{m}$ , diameter of approximately 800 nm, and a mushroom-shaped cap of  $\sim 2 \mu\text{m}$  in diameter. Parameters and electroplating solution are chosen to generate a rough texture of the mushroom head, which increases its effective surface and adhesion to cell membrane (Fig. 3.2g). Next, a layer of silicon oxide ( $\sim 3,000 \text{ \AA}$ ) is deposited by CVD processing.

Another layer of photoresist is applied for a final lithographic step to expose the contact pads and the heads of the gold mushrooms, followed by wet oxide etch to selectively remove the oxide from the contact pads and the mushroom heads. Wafers are sawed and undergo manual bonding to a 62-pad printed circuit boards to which 21 mm glass rings are attached to create a recording bath chamber for in vitro recording.

### 3.2.2 *Chemical Functionalization*

In contrast to the classical approach of having to forcefully push microelectrodes into the cells, we induced engulfment of the gM $\mu$ E by the cell using a peptide that triggers processes of phagocytosis at the cell–gM $\mu$ E point of contact. Phagocytosis is a conserved cell-biological mechanism for the internalization of particles [54]. Processes of endocytosis and phagocytosis are known to be mediated by integrins and RGD-based ligands [55] whose participation in processes of cell-matrix adhesion is also well established [56]. We have found that the peptide that induces engulfment of the gM $\mu$ E by the cell most efficiently is a cysteine (C)-terminated peptide with a number of RGD repeats and a long decalysine (K<sub>10</sub>) spacer: CKKKKKKKKKPRGDMPRGDMPRGDMPRGDM (MW 3,630 g/mol) [48, 49]. This peptide was referred to as the engulfment promoting peptide (EPP) and was covalently linked to the surface of the device. Functionalization of the gM $\mu$ E gold surface with the cysteine-terminated peptide makes use of thiol–gold monolayer self-assembly and is done by direct application of the peptide onto the surface (1 mM in phosphate buffer saline at room temperature, overnight). The glass surface in between the gold mushrooms underwent surface functionalization using 3-aminopropyltrimethoxysilane (APTMS, Aldrich, 1 % in MeOH, 10 min in room temperature) to introduce terminal amine groups to the glass surface. Samples were then washed with MeOH to remove uncoupled APTMS. The protein immobilization linker 4-Maleimidobutyric acid sulfo-N-succinimidyl ester (sGMBS, Sigma, 0.5 % in PBS) was then applied to the surface and washed with PBS after 40 min at room temperature. EPP peptide was then applied to the surface and left for 24 h in which the cysteinic thiol residue reacted with the maleimido part of the anchored linker. Samples were then washed with PBS.

## 3.3 Analysis of Cell–gM $\mu$ E Interface

### 3.3.1 *Ultrastructural Studies of Cell–gM $\mu$ E Junction*

Using transmission electron microscopy (TEM), we have found that different cell types, including *Aplysia* neurons, rat hippocampal neurons, Chinese hamster ovary cells (CHO), embryonic fibroblast cells (NIH/3T3), rat adrenal medulla cells

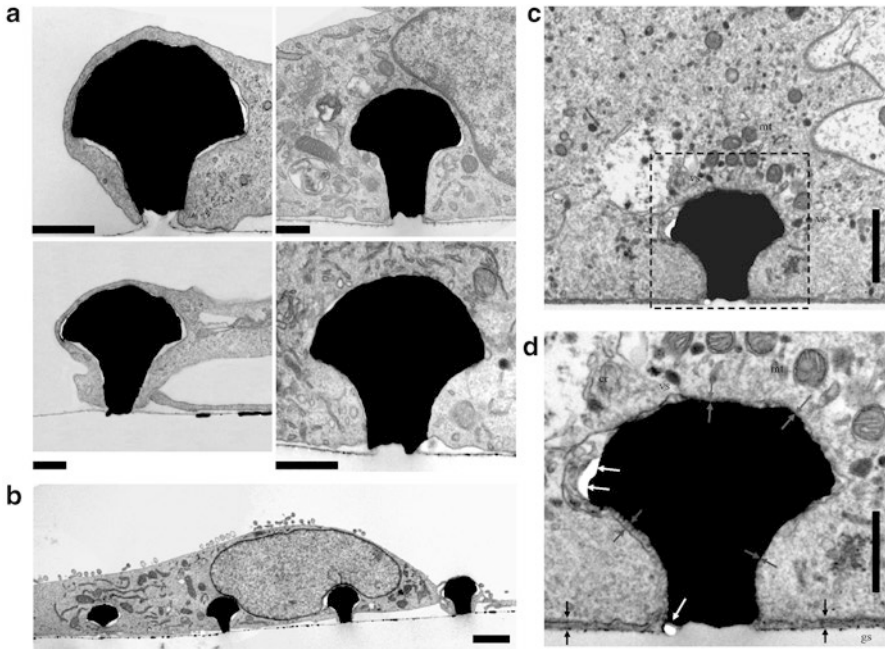


**Fig. 3.3** Transmission electron microscopic images of gM $\mu$ Es engulfed by various cell types. (a) CHO, fibroblasts (3T3), cardiomyocytes (H9C2), and rat adrenal medulla cell lines (PC-12). Scale bars, 500 nm. (b) Engulfment of multiple gM $\mu$ Es by a 3T3 cell. Scale bar, 2  $\mu$ m. (c, d) *Aplysia* neuron engulfing a gM $\mu$ E coated with EPP. The gap formed between the plasma membrane and the flat surface is 30–50 nm (black arrows). The gap between the gM $\mu$ E structure and the plasma membrane is less than 30 nm, and in some areas, it cannot be defined and seems to be zero (gray arrows). White arrows indicate regions where the embedding polymer was torn most probably by post-embedding mechanical tension, as the quality of the fixation is evident by the preservation of the organelles (mt mitochondria, vs vesicle, er endoplasmic reticulum, gs area of flat gold substrate). Scale bars, 1  $\mu$ m and 500 nm. Reproduced from [48] © The Author(s)

(PC-12), and rat myocardium cells (H9C2), all engulf functionalized gM $\mu$ Es [48, 57, 58].

Cells grown on flat glass cover slides coated by poly-L-lysine (PLL) adhere to the substrate forming a cleft with a thickness of  $55.8 \pm 28.9$  nm, while occasionally the cleft dimension can be larger than 100 nm [48, 59]. When grown on a matrix of gM $\mu$ Es coated with EPP (Fig. 3.3), cells engulf the protruding gM $\mu$ E, forming intimate contact with a considerably smaller cleft thickness (Fig. 3.3c, d, and see [48, 58]). For example, the average width of the cleft formed between the plasma membrane of cultured *Aplysia* neurons and the flat substrate between the gM $\mu$ Es is  $56 \pm 29$  nm, while an average cleft width of  $35 \pm 21$  and  $30 \pm 17$  nm is observed between the gM $\mu$ E head and stalk, respectively (Table 3.1). Moreover, in many of the electron micrographs, the plasma membrane appears to be in direct contact with the gM $\mu$ E head and stalk (i.e., without a discernible space between the

**Table 3.1** Average width values (nm) of the cleft formed between the plasma membrane of various cell types and the flat gold surface in between the gM $\mu$ Es, gM $\mu$ E stalk, and gM $\mu$ E head, according to the analysis of transmission electron microscopy images

	Flat surface (nm)	gM $\mu$ E stalk (nm)	gM $\mu$ E head (nm)	F-value
Aplysia	55.8 $\pm$ 28.9	35.2 $\pm$ 20.8	30 $\pm$ 16.7	F <sub>(2,357)</sub> =43.5, p<0.001
CHO	89.0 $\pm$ 66.4	31.2 $\pm$ 27.6	8.5 $\pm$ 16.3	F <sub>(2,357)</sub> =89.6, p<0.001
3T3	80.1 $\pm$ 63.1	37.5 $\pm$ 35.1	15.7 $\pm$ 10.2	F <sub>(2,447)</sub> =90.7, p<0.001
H9C2	122.8 $\pm$ 74.5	49.2 $\pm$ 41	49.8 $\pm$ 32	F <sub>(2,447)</sub> =97.6, p<0.001
PC-12	144.8 $\pm$ 117.6	31.4 $\pm$ 27.6	26.9 $\pm$ 24	F <sub>(2,447)</sub> =132.4, p<0.001

The fifth column depicts the significance of the difference between average cleft width values of the different areas examined (analyzed using one-way ANOVA). Reproduced from [48]

© The Author(s)

**Table 3.2** Percentage of the areas where the cleft width is in the range of 0–10 nm in various cell types

Cell type	Flat surface (%)	gM $\mu$ E stalk (%)	gM $\mu$ E head (%)
Aplysia	0	10	12.5
CHO	0	14.2	24.2
3T3	0.7	18.7	35.3
H9C2	0.6	4	7.3
PC-12	0	10	10.7

plasma membrane and the gold surface; see Fig. 3.3d, gray arrows), suggesting a significantly tighter seal between the plasma membrane and the gM $\mu$ E compared with the flat surface between the gM $\mu$ Es. In fact, an estimated 10 % of the contact area between the plasma membrane and the gM $\mu$ E stalk and 12.5 % of the contact area with the gM $\mu$ E head form close adhesion with the cleft width in the range of 0–10 nm (Table 3.2). The cleft formed between the flat substrate (in between the gM $\mu$ Es) and the cell membrane rarely reaches values smaller than 10 nm (Table 3.2) despite the large variability observed (56 $\pm$ 29 nm; also see Table 3.1 for other cell types).

The seal resistance ( $R_{seal}$ ) formed at the cleft between the neuron and the sensing element of the electronic device is a major limiting factor for effective electrical recordings (for review, see [40]).  $R_{seal}$  depends on the width of the cleft ( $d_c$ ), the resistivity of the material within the cleft ( $\rho_c$ ), and its planar dimensions.  $R_{seal}$  can therefore be calculated according to

$$R_{seal} = \frac{\rho_c}{2\pi \cdot r \cdot d_c} \cdot l \quad (3.1)$$

where  $r$  is the radius of the gM $\mu$ E head, taken as 0.95  $\mu$ m, and  $l$  is the length of the resistor across which the transductive extracellular current flows and is taken as the axial circumference of the gM $\mu$ E (approx. 4  $\mu$ m). Assuming the specific resistance of the cleft  $\rho_j$  to be 100  $\Omega$  cm (electrolyte solution), we arrive at  $R_{seal} > 67$  M $\Omega$  for cleft width  $d_j < 10$  nm. The seal resistance formed between cultured *Aplysia* neurons and a flat substrate was found to be 1.2 $\pm$ 0.43 M $\Omega$  [60]. Thus, our estimation suggests that the neuron–gM $\mu$ E junction improves  $R_{seal}$  by at least 50-fold.

It should be noted that using TEM to assess the nature of the extracellular cleft formed between the plasma membrane of living cells and artificial substrates must be done with great caution as the procedures of chemical fixation, dehydration, embedding, and sectioning might generate alterations in the intracellular osmotic pressure and thereby generate structural artifacts [61]. Nevertheless, as is evident from the well-preserved structure of the mitochondria, vesicles, the endoplasmic reticulum, and the plasma membrane facing the bathing medium (Fig. 3.3d) in the electron micrographs, the fixation, dehydration, and embedding procedures did not produce osmotic pressure artifacts. The presence of electron translucent breaks within the embedding material, mainly (but not exclusively) at the curving junctions between the cells and the gM $\mu$ E head as well as the stalk (e.g., Fig. 3.3d, white arrows), suggests that mechanical tension generated within the embedding polymer (Agar 100) leads to the detachment of the plasma membrane from the surface of the gM $\mu$ E head only during sectioning of the agar block or the observations rather than at earlier stages of the procedures.

### 3.3.2 *Live Confocal Imaging of Actin Cytoskeleton at the gM $\mu$ E–Neuron Junction*

The difference in the cleft width formed at the neuron–gM $\mu$ E interface and the neuron–flat-substrate interface as seen in TEM could result from mechanical stretching of the plasma membrane around the gM $\mu$ E head by cytoskeletal elements that assemble around these structures. In order to assess whether the engulfment of the functionalized gM $\mu$ E is mediated by actin and other submembrane cytoskeletal elements and molecular motors, we used confocal imaging of fluorescent probes in live *Aplysia* neurons grown on matrices of gM $\mu$ Es [49].

Neurons cultured on gM $\mu$ E matrices functionalized by either PLL or EPP were fluorescently labeled by expression of GFP fusion proteins. Initially we expressed GFP alone, thereafter because of the important role of actin in focal adhesion formation [56], and in the generation of the mechanical forces associated with phagocytosis [62], we expressed GFP–actin by microinjection of mRNA encoding for GFP–actin. Expression of GFP–actin in cultured *Aplysia* neurons generates a diffuse signal in the cytosol in association with the homogeneous distribution of globular actin, GFP–actin hotspots in association with focal adhesion, and high-intensity fluorescent GFP–actin stripes in association with F-actin [63, 64]. Confocal microscope scans of 0.2  $\mu$ m steps on the Z-axis were taken approximately 24 h after injection, and three-dimensional (3D) computer-aided reconstructions were prepared (Fig. 3.4). This procedure revealed that in both EPP- and PLL-functionalized matrices, the cell body and the main axon engulfed many gM $\mu$ E but to variable degrees: clear differences in engulfment were observed with respect to the coating used as full and tight engulfment of the head and stalk is significantly more frequent on EPP- compared with PLL-coated substrates (Fig. 3.4d–f). Moreover, intense GFP–actin fluorescent signal in the form of a complete or partial “actin ring” was

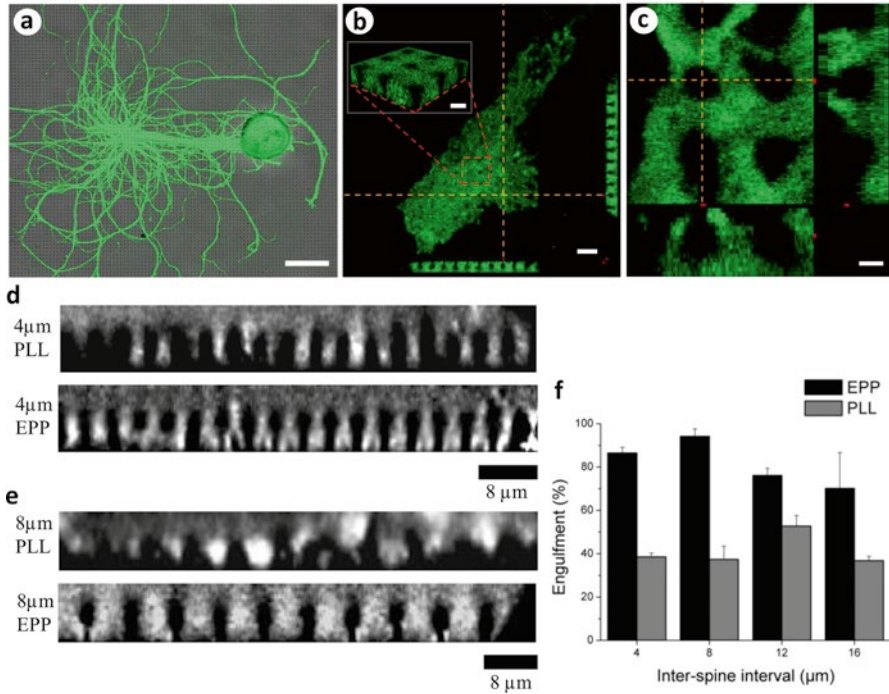


**Fig. 3.4** Confocal microscope images of neurons expressing GFP-actin engulfing gMμEs. (a) An overview of a neuron cultured on 8 μm spaced gMμE matrix. The image is constructed of superpositioning of transmitted light and confocal GFP-actin images. (b) A confocal image taken 0.4 μm above the substrate surface. The equally spaced black dots depict single gMμEs. *Inset*: a computer-generated 3-dimensional reconstruction from a series of optical sections. (c) Zoom-in of a single PLL-coated gMμE engulfed by the neuron. Scale bars, 100 μm in (a), 10 μm for (b), 5 μm (b, *inset*), and 2 μm (c). The dashed lines denote plane of scan in both (b) and (c). (d, e): comparison of the engulfment of EPP- and PLL-functionalized gMμEs by neurons. Z-axis scans of the cell bodies of neurons cultured on a 4 μm (d) and 8 μm (e) inter-gMμE intervals. (f) Quantitative analysis of the engulfment of EPP-coated (black) and PLL-coated gMμE matrices (gray) as viewed from z-scans of GFP-actin expressing neurons. Scale bars, 8 μm. Reproduced with permission from [49], © (2009) IOP Publishing

frequently detected surrounding the stem of the EPP-functionalized gMμE (Fig. 3.5), as compared with PLL-coated substrate where hotspots of actin were dispersed in a non-organized fashion throughout the plane of cell-substrate interface in between gMμEs (Fig. 3.5b, d).

We decided to examine the assembly of specialized protein structures around the stalk of the gMμEs using an additional molecular probe, namely, cherry-cortactin. Cortactin is an F-actin-associated protein that regulates actin assembly at multiple binding sites and serves mainly as a stimulator of actin nucleation and branching by activation of Arp2/3 [65]. Cells cultured on EPP-coated matrices and injected with cherry-cortactin displayed ring-shaped cortactin fluorescence surrounding the

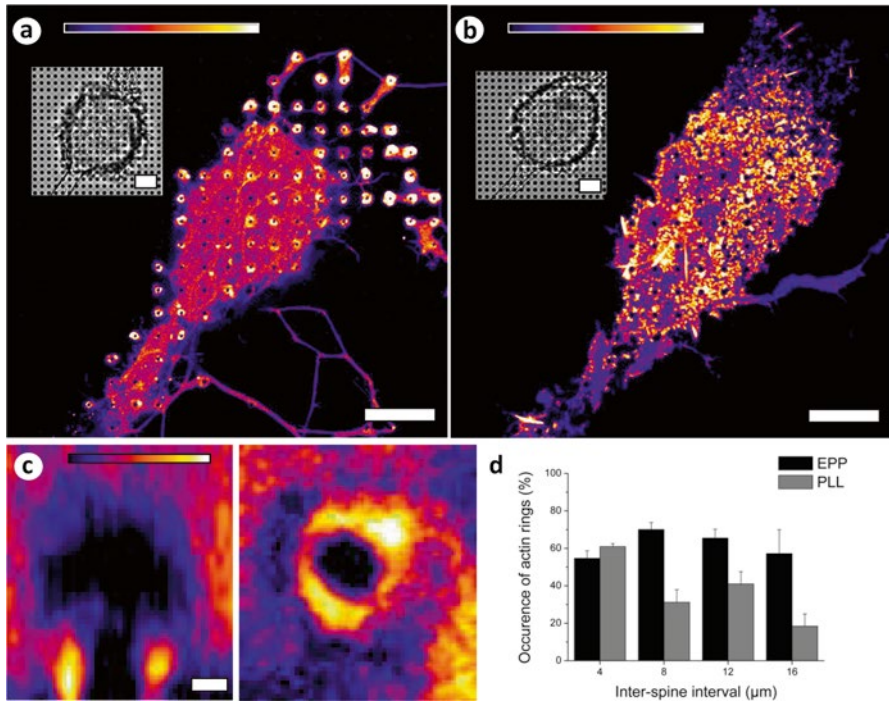


**Fig. 3.5** Occurrence of “GFP–actin rings” surrounding the stems of EPP- and PLL-coated gM $\mu$ Es. (a) and (b) depict the cell somata of *Aplysia* neurons cultured on EPP- and PLL-coated 8  $\mu\text{m}$  spaced gM $\mu$ E matrices, respectively. Relative intensity scale of the GFP–actin is shown at the top of both (a) and (b). Images were taken at the plane of the gM $\mu$ E stem. *Insets*: corresponding transmitted light images of the cell bodies. Scale bars, 25  $\mu\text{m}$ . (c) A ring of GFP–actin signal surrounding the stem of a gM $\mu$ E. *Left-hand side*, ZX-axis scan; *right-hand side*, XY-axis scan taken at the plane of the gM $\mu$ E stem (scale bar, 1  $\mu\text{m}$  for both scans). (d) Comparison of the occurrence of actin rings surrounding the stems of gold spines on 4, 8, 12, and 16  $\mu\text{m}$  matrices, coated with either EPP (black) or PLL (gray). Reproduced with permission from [49], © (2009) IOP Publishing

gM $\mu$ E stalks, and in addition, when co-expressed, actin and cortactin fluorescence were generally colocalized [49].

These findings show that the gM $\mu$ Es functionalized with EPP promote engulfment and actin polymerization around the stalk of the gM $\mu$ E. Interestingly, in EPP actin rings are dominantly formed around the stalk, whereas the actin density along the substrate and the head of the gM $\mu$ E is small (Fig. 3.5a, c). This suggests that in addition to the chemical signaling generated by the EPP, the mechanical tension generated by the geometry of the gM $\mu$ Es also provides meaningful information for actin assembly, as is consistent with other studies [56]. However, as PLL alone does not generate tight engulfment of the gM $\mu$ Es by the neurons, the geometry of the gM $\mu$ Es is not sufficient by itself to trigger specific interactions between the cell and substrate.

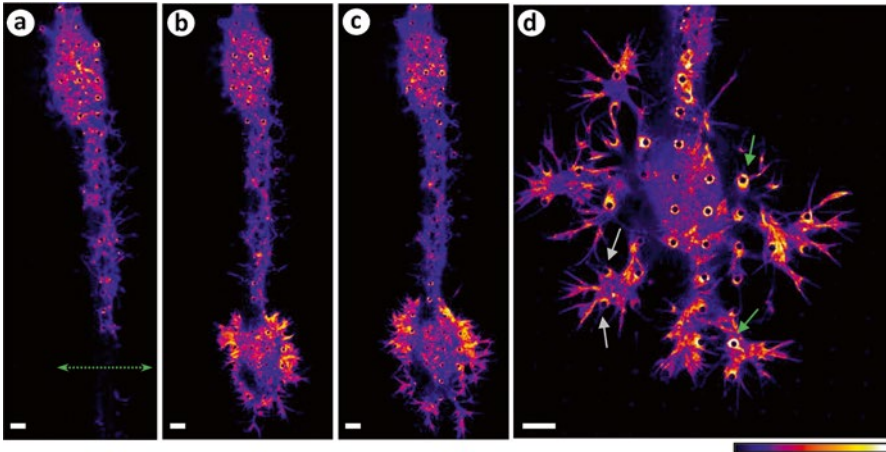


**Fig. 3.6** Growth cone extension of transected axon on EPP-coated 8  $\mu\text{m}$  spaced gM $\mu\text{E}$  matrix. (a) Shown are the cell body (*upper part*) and its axon. Axotomy was applied along the double-headed arrow leading to the formation of a growth cone in the form of an extending flat lamellipodium (*lower part* of the images in **b–d**). (b) Ten minutes after axotomy, (c) twenty-two minutes, and (d) thirty-two minutes post axotomy. In (c), two arrows on the right indicate accumulation of GFP-actin in the form of rings around the stem of a gM $\mu\text{E}$ . Two arrows on the left indicate advancing lamellae in the process of forming actin rings (scale bars, 10  $\mu\text{m}$ ). Reproduced with permission from [49], © (2009) IOP Publishing

The observation that the engulfment of gM $\mu\text{E}$ s is associated with the assembly of GFP-actin rings around the stalk raised a number of questions. How fast does an actin ring assemble after the plasma membrane comes in contact with the gM $\mu\text{E}$ ? Given that the cytoskeletal elements are generally dynamic structures and that actin skeleton associated with adhesion plaques is highly dynamic [66], how stable are the formed actin rings?

To study the dynamics of actin ring assembly, we took advantage of earlier observations from our laboratory showing that axonal transection of cultured *Aplysia* neurons results in the formation of a growth cone in the form of an extending flat lamellipodium at the tip of the cut axon (for review, see [67]). The extension of a lamellipodium within 10–20 min after axotomy provides an opportunity to image the kinetics of GFP-actin ring formation during the first interaction of the plasma membrane with a functionalized gM $\mu\text{E}$ . We found that within 2–12 min of contact between the flat lamellipodium and a gM $\mu\text{E}$ , distinct actin rings are assembled (Fig. 3.6). Using a criterion of ring integrity (>75 % of the gM $\mu\text{E}$  stalk is surrounded by circular high fluorescent GFP-actin), we found that 48 h after plating, the actin rings are dynamic: a single actin ring disappears and reappears at an average frequency of  $4 \cdot 10^{-3} \text{ Hz} \pm 0.2 \cdot 10^{-3}$ . Imaging the actin-ring temporal dynamics once a day over a period of 10 days revealed that even though the number of gM $\mu\text{E}$ s enwrapped by actin rings remains unchanged, the actin-ring temporal dynamics are significantly reduced [49].

The formation of non-static actin rings at the stalk of the gM $\mu$ Es suggests that the actin cytoskeleton is being constantly remodeled around the protruding structures in response to the extracellular chemical and mechanical signals. This process could be a result of nucleation of new actin filaments and/or consecutive repolymerization and depolymerization of existing actin filaments [68] similarly to adhesion processes occurring at the leading edge of motile or growing cells. We have also shown that the dynamic nature of rings of actin stabilizes around the stalks of the gM $\mu$ Es approximately 2 weeks after culturing. This might correlate to common behavior of cells in vitro, where they often reach a structural steady state after a certain amount of time [69]. The dynamic nature of actin has also been observed at developing synapses of CA1 pyramidal neurons in rat hippocampal slices [70] where photoactivated GFP-actin was used to assess F-actin turnover rate in plastic dendritic spines. In that study, it was shown that actin exists in distinct pools, with a turnover rate of tens of seconds for the dynamic pool and minutes for the stable pool, not unlike the aforementioned observations. Additionally, previous studies show that monomeric G-actin is constantly being polymerized into ring-shaped networks of F-actin in endocytic hotspots of lamprey synapses [71, 72]. Although in these studies it was demonstrated that the actin rings at areas of vesicle recycling are stable, it was shown nonetheless that there is a constant dynamic turnover as is evident by the application of actin depolymerizing toxin latrunculin B which prevents the incorporation of G-actin into the F-actin rings. Could the dynamic nature of the cytoskeleton at the vicinity of the gM $\mu$ E reflect the formation of presynaptic structures? In light of the dynamic reorganizing nature of actin and cortactin surrounding the stalks of the gM $\mu$ Es, it should be no less than exciting to check for the existence of synaptic-related proteins [73] in the area of interaction between the neurons and the gM $\mu$ E.

### 3.4 In-Cell Recording and Stimulation

Ultrastructural studies and live confocal imaging demonstrate a tight and active interface between cells and gM $\mu$ Es. We now turn to the electrical implications of this tight seal. We will explore the ability of gM $\mu$ Es to provide simultaneous, multisite, long-term stimulation and recording of action potentials and subthreshold synaptic potentials. We will show signal quality and signal-to-noise ratio comparable to that of conventional intracellular glass micropipette electrodes while maintaining scalable design options of multielectrode devices. This section is based on published studies [50–52] in which further technical information can be found.

#### 3.4.1 *In-Cell Recording of Action Potentials and Membrane Hyperpolarization*

The experiment described in Fig. 3.7 (also described in [50]) depicts the main features of the “in-cell recording” configuration. For the experiment, an *Aplysia*

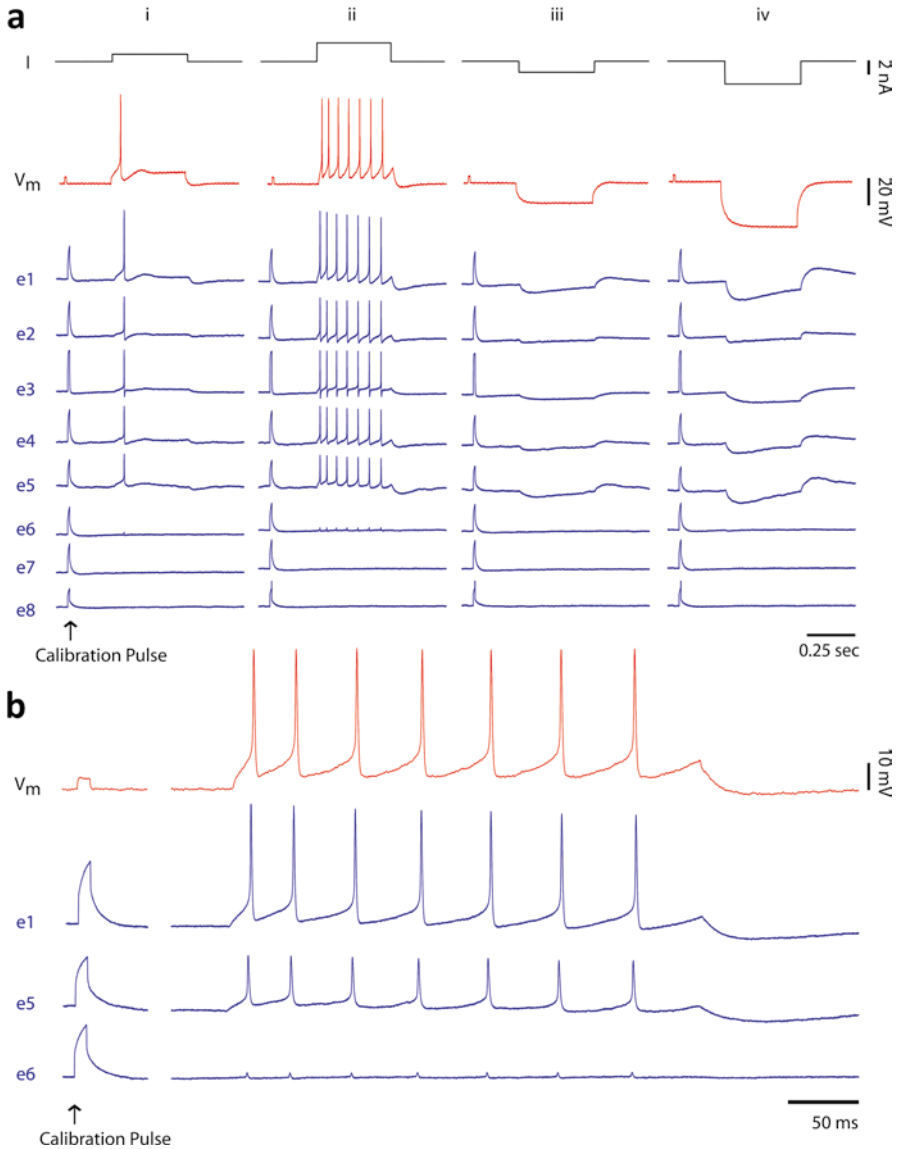


**Fig. 3.7** In-cell recording of action potentials and subthreshold hyperpolarizing pulses by gM $\mu$ Es. A neuron was cultured for 2 days on a gM $\mu$ Es array device. Recordings of action potentials and hyperpolarizing pulses generated by an intracellular glass microelectrode inserted into the soma were made from eight gM $\mu$ Es (*e1–e8*). Six gM $\mu$ Es reside under the neuron (*e1–e6*) and two away from it (*e7* and *e8*). (a) A 5 mV, 10 ms square calibration pulse is delivered at the onset of each voltage trace. Depolarizing current pulses injected through the intracellular electrode (a, *i* and *ii*) generated membrane depolarization which reached threshold to fire a single action potential (*i*) and a train of action potentials (*ii*). These action potentials were recorded by gM $\mu$ Es *e1–e6*. The trace showing the trains of action potentials recorded by the intracellular electrode and gM $\mu$ Es *e1*, *e5*, and *e6* in (*ii*) are enlarged in (b). Note the differences in the shapes and amplitude of the 5 mV 10 ms calibration pulses and the action potentials. In columns *iii* and *iv*, hyperpolarizing square pulses were delivered by the intracellular glass microelectrode. The different degrees of electrical coupling between the neuron and the gM $\mu$ Es and the differences in the filtering of the DC pulse by the different gM $\mu$ Es are apparent (*ii* and *iv*). Reproduced from [50] © The Author(s)

neuron was cultured for 2 days on an array of 62 gM $\mu$ Es functionalized with the engulfment promoting peptide (EPP). A sharp-glass microelectrode for both current injection and voltage recording was inserted into the soma of the neurons. Depolarizing current pulses of varying intensities (Fig. 3.7a, columns *i* and *ii*) were delivered by the intracellular electrode and generated a single or a train of action potentials recorded by the same glass microelectrode and the gM $\mu$ Es. The action potentials recorded by the gM $\mu$ Es were monophasic, positive potentials that resemble in shape the intracellularly recorded action potentials (APs, Fig. 3.7a, b). In this experiment, APs were recorded by six gM $\mu$ Es that resided beneath the stimulated neuron's cell body (Fig. 3.7, *e1–e6*, blue). The amplitudes of the raw APs recorded by *e1–e5* were in the range of 5–10 mV, while those recorded by *e6* were smaller than 1 mV, reflecting differences in the electrical coupling between the neuron and the individual gM $\mu$ Es. Interestingly, even the small APs of *e6* were positive monophasic potentials. Other gM $\mu$ Es not residing beneath the neuron's cell body did not record any signals (*e7*, *e8*). This fact demonstrates the lack of cross-talk artifacts from neighboring microelectrodes. Using the same configuration, we recorded in other experiments monophasic action potentials with amplitudes of up to 25 mV [51].

Hyperpolarizing pulses of increased amplitude delivered by the intracellular microelectrode generated membrane hyperpolarization (Fig. 3.7, columns *iii* and *iv*) that were picked up also by gM $\mu$ Es *e1–e6*. This clearly demonstrates that the interface formed between the neuron and the gM $\mu$ E generates electrical coupling sufficient to enable parallel multiple site recordings of APs and subthreshold potentials.

### 3.4.2 In-Cell Recording of Subthreshold Synaptic Events

To further illustrate the quality of the recording provided by the gM $\mu$ E-based microelectrode array, we cocultured homologous *Aplysia* neurons that form electrical synapses [74]. Figure 3.8 depicts an experiment performed on two neurons cultured on a gM $\mu$ E array for 2 days. For the experiment, a sharp-glass microelectrode for both current injection and voltage recording was inserted to neuron 1, and recordings were made with a gM $\mu$ E from neuron 2 (Fig. 3.8a). Hyperpolarizing square current pulse delivered to neuron 1 generated membrane hyperpolarization of neurons 1 and 2 (Fig. 3.8b). The coupling coefficient (the algebraic scaling factor) between neuron 1 (as recorded by an intracellular DC-coupled electrode) and the raw signal recorded in neuron 2 (by the AC-coupled gM $\mu$ E, Fig. 3.8biii) was estimated to be 0.2–0.3. Consistent with these observations, firing of neuron 1 (Fig. 3.8cii) generated an excitatory postsynaptic potential (EPSP) in neuron 2 (Fig. 3.8ciii) which reached threshold to initiate an AP (Fig. 3.8ciii). The AP in neuron 2 (Fig. 3.8ciii) in turn initiated an EPSP in neuron 1 (Fig. 3.8cii). Trains of action potentials generated by the intracellular electrode in neuron 1 (Fig. 3.8c, right column) generated a train of EPSPs in neuron 2 that summated to fire a train of action potentials (Fig. 3.8c right panel).

It is important to note that the impedance of the gM $\mu$ Es and the AC amplifiers used for the recording by the gM $\mu$ E alter the shape of the recorded signals compared

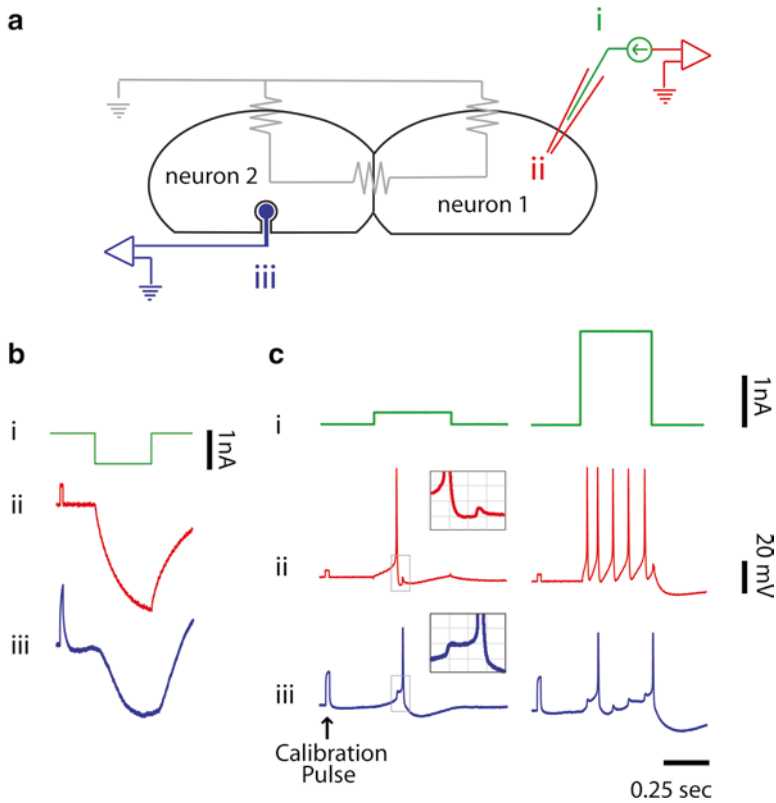


**Fig. 3.8** In-cell recording of subthreshold synaptic potentials. (a) Experimental setup. (b) Hyperpolarizing square current pulse (*i*) delivered to cell 1 (*right-hand side* in **a**), generated membrane hyperpolarization of both cells 1 and 2, and picked up by the glass micropipette electrode and the gM $\mu$ E (**b** *ii* and *iii*, respectively) demonstrating the electrical coupling between the cells. (c) Depolarizing square current pulse (*i*) delivered to cell 1 elicited firing of an action potential (*c* *ii*) and generated an excitatory postsynaptic potential (EPSP) in cell 2 picked up by the gM $\mu$ E (**c** *iii*). The AP in cell 2 (**c** *iii*) in turn initiated an EPSP in cell 1 (**c** *ii*) (*insets*: close-up of concurrently recorded EPSPs and APs in both cells). Trains of action potentials (*right-hand-side* panels) generated by the intracellular electrode in cell 1 generated a train of EPSPs in cell 2 (*iii*) that summated to fire a train of action potentials. Reproduced from [50] © The Author(s)

with those recorded by the DC-coupled intracellular sharp-glass electrode. The electrical impedance depends on the ionic bilayer (also known as the electrical double layer) [75] formed at the interface between the gM $\mu$ E and the culture medium and of the AC amplifier used. In addition, the attenuation in the amplitude is further attributed to the quality of the seal resistance formed between the plasma membrane and the gM $\mu$ E and the conductance of the patch of plasma membrane that faces the gM $\mu$ E. Since the parameters that represent individual neuron–gM $\mu$ E junction are not identical, the alterations in the signal shape and attenuation factor differ for individual gM $\mu$ Es, as is reflected by the differences in the shapes and amplitude of

the 5 mV 10 ms calibration pulses and the action potentials (Fig. 3.7). Nevertheless, these individual alterations can be corrected using the calibration pulse as a reference and employing either an offline or a real-time negative capacitance compensation circuit [51, 76, 77]. Thus, in spite of the filtering and attenuation of the signals by the gM $\mu$ E impedance and AC-coupled amplifier, the quality of recording by the extracellular positioned gM $\mu$ E is of unprecedented quality.

### 3.4.3 *In-Cell Stimulation*

Analysis of neuronal circuits largely relies on repeated use of stimulating electrodes. It is of critical importance that stimuli are delivered without damaging the cells [78]. Whereas current injection (stimulation) by intracellular sharp-glass electrodes or patch electrodes involves no difficulty, stimulation by extracellular high-impedance electrodes is complicated by the relatively limited charge transfer to the plasma membrane, by the risk of damaging the cells by electroporation [7, 79, 80], or by irreversible electrochemical reaction products [81–84]. To overcome these problems, trains of weak capacitive stimuli can be delivered to cultured cells to activate local sodium currents that generate sufficient depolarization to reach the firing threshold [78]. While this approach is safe, it might complicate experimental protocols in which precisely timed consecutive stimuli are to be delivered.

We now examine whether the interface formed between the gM $\mu$ Es and the neurons as well as the gM $\mu$ E properties supports effective stimulation of the neurons without inducing irreversible electroporation. To that end, a neuron cultured on a gM $\mu$ E-based microelectrode array was impaled by a sharp electrode for both current injection and voltage recordings (Fig. 3.9). We next characterized the coupling level between the neuron and the gM $\mu$ E and selected to concentrate on two gM $\mu$ Es, one with high coupling (gM $\mu$ E-1) and the other with low coupling values (gM $\mu$ E-2) (Fig. 3.9a). Hyperpolarization of the neuron by current injection through the intracellular electrode leads to gM $\mu$ E-1 and to a much smaller extent gM $\mu$ E-2 (Fig. 3.9b*i*). Consistently, depolarization of the neuron to fire an action potential leads to the generation of an action potential of  $\sim 3$  mV recorded by gM $\mu$ E-1 and  $\sim 0.5$  mV by gM $\mu$ E-2 (Fig. 3.9c*i* and *d**i*, respectively). Delivering a single depolarization square voltage step of 1–10 ms with an increasing voltage from 1,400 to 1,800 mV by gM $\mu$ E-1 evoked depolarization of the neuron which reached threshold to fire action potentials as recorded by the glass microelectrode (Fig. 3.9e, upper panel). Applying similar current pulses to gM $\mu$ E-2 depolarized the neuron but failed to reach threshold (Fig. 3.9e, bottom panel).

To examine whether this series of stimulations (5–10 stimulations per experiment) via the gM $\mu$ E induced damages to the neuron, we once again delivered hyperpolarizing pulses through the intracellular glass microelectrode and measured the input resistance and the coupling between the neurons and the gM $\mu$ Es. As seen in Fig. 3.9 (*b**ii*, *c**ii*, and *d**ii*), the stimuli delivered by the gM $\mu$ E did not induce detectable changes to the neuron's input resistance or altered the coupling coefficient between the neuron and the gM $\mu$ E.

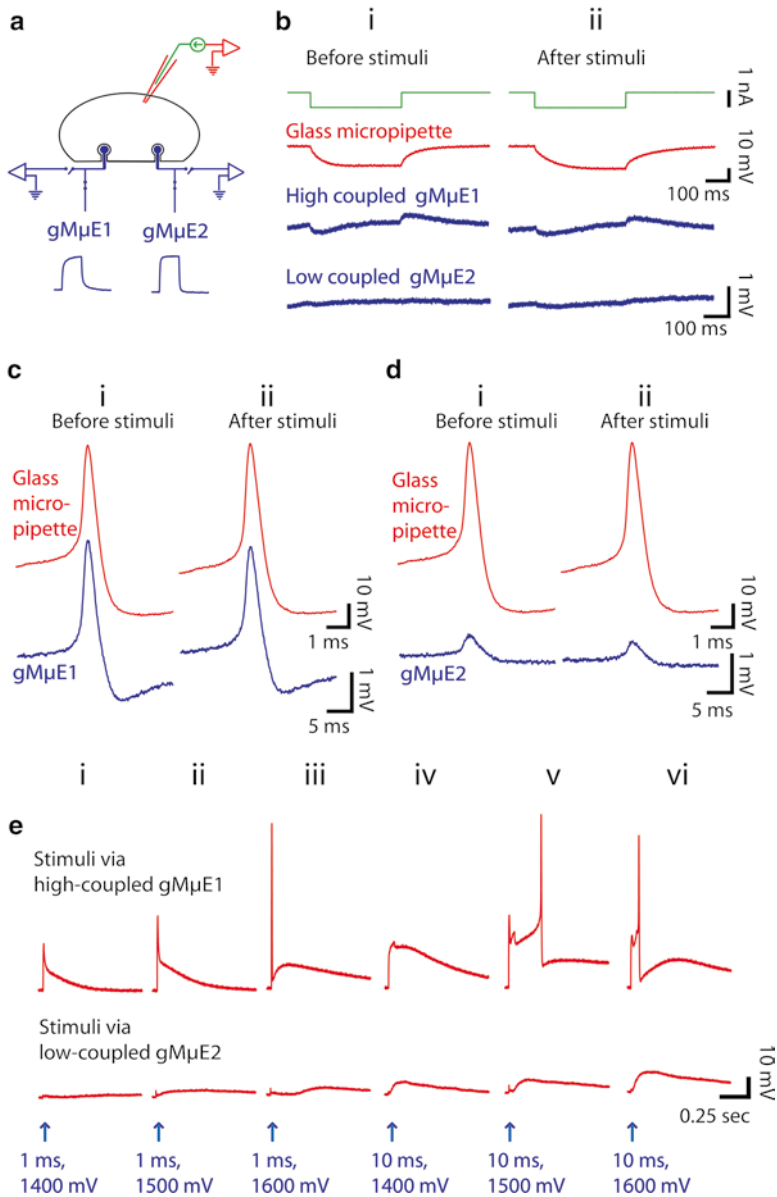
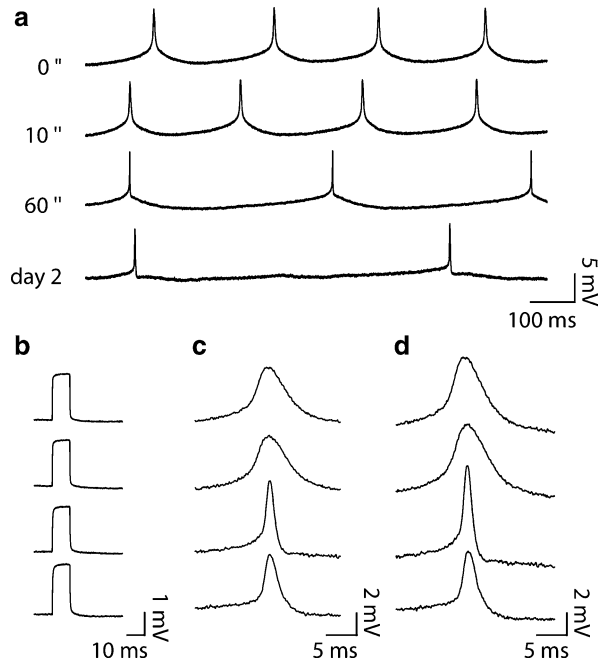


**Fig. 3.9** Stimulation by gMμEs without damage to the cell. **(a)** Experimental setup. **(b)** Hyperpolarizing square current pulse delivered to the cell by the glass micropipette intracellular electrode generated membrane hyperpolarization detected by both high- and low-coupled gMμEs (gMμE1 and gMμE2, respectively, in *i*). The input resistance and level of coupling between the neuron and gMμE1 and gMμE2 were not changed before and after the application of stimuli delivered by gMμE1 and gMμE2 stimulation (shown in **e**). **(c, d)** Action potential shape, duration, and amplitude as recorded by gMμE1 and gMμE2. These are not changed by the use of gMμE1 and gMμE2 to stimulate the neuron (shown in **e**). **(e)** Stimulation of the neuron by gMμE1 and gMμE2 while recording with the intracellular glass microelectrode. The strength of the applied stimulus and its duration are given below the traces. Note that whereas the high-coupled gMμE1 (*upper* panel) generated an action potential, the low-coupled electrode did not reach threshold. Reproduced from [50] © The Author(s)

**Fig. 3.10** Long-term in-cell recording from a spontaneously active neuron. (a) Recording sessions from the same neuron of hours and days are maintained (time is given on the *left-hand side*). (b) Calibration pulse along 2 days of recordings. (c) The shapes and amplitudes of the raw action potentials recorded by gM $\mu$ E<sub>s</sub> along 2 days. (d) Deconvolution of the recorded action potentials using the calibration pulses and a capacitance compensation circuit (see [51]). Reproduced from [50] © The Author(s)



We conclude that with the observed high coupling coefficient, the in-cell configuration enables the application of sufficient current to reach firing threshold of the neuron without inflicting damages to the plasma membrane or the junction.

#### 3.4.4 Stability of the gM $\mu$ E–Neuron Junction

A critical feature of the extensive use of extracellular recording for in vitro and in vivo research purposes as well as for potential future clinical applications is the cell-noninvasive nature of the electrodes which permits long-term recordings. In an earlier study, we established that culturing *Aplysia* neurons on a dense matrix of gold mushroom-shaped protrusions (gM $\mu$ Ps) for over a week does not alter the excitable membrane properties and synaptic physiology of the neurons [48]. We now turn to examining the functional stability of the junctions formed between the neurons and the gM $\mu$ E. We began to examine this question by culturing spontaneously active *Aplysia* neurons on gM $\mu$ E-based microelectrode arrays (Fig. 3.10 and see [50]). We found that effective electrical coupling between neurons and gM $\mu$ E<sub>s</sub> was maintained for over 48 h. It should be noted that in these experiments, the shape and amplitude of the action potentials over this period were not absolutely stable. We avoided the risk of culture contamination by not taking off the cover from the culture dish for insertion of a conventional sharp intracellular

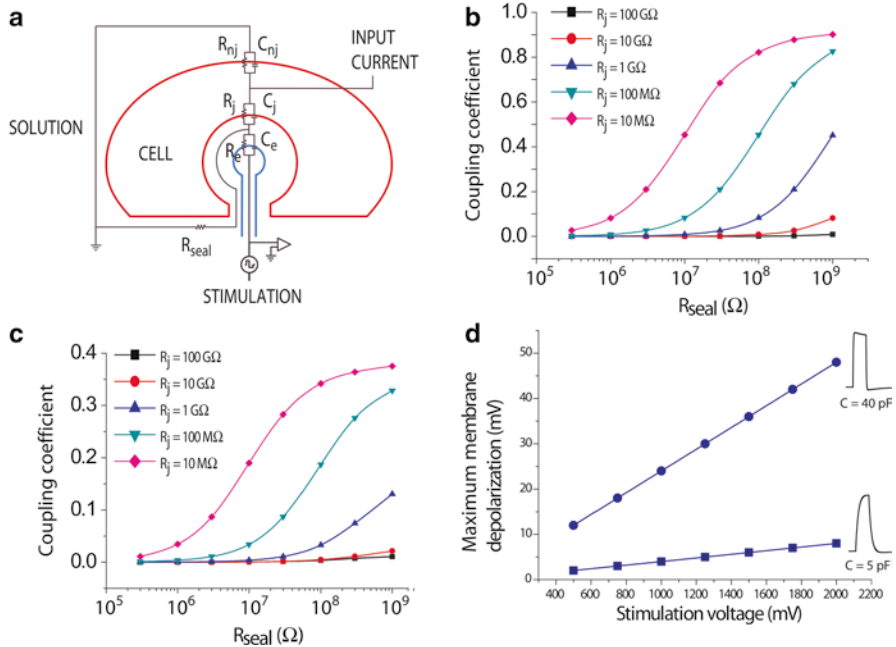


**Fig. 3.11** The in-cell configuration: ohmic conductance at the junctional membrane. (a) Equivalent circuit of gMμE–neuron junction. (b) and (c): coupling coefficient as a function of seal resistance and the resistance of the junctional membrane in high-frequency (100Hz) (b) and low-frequency (1Hz) (c) signals. (d) In-cell stimulation: maximum membrane depolarization as a function of amplitude of voltage-based stimulation through the gMμE in high (circles) and low (squares) capacitance gMμEs. Application of an  $\sim 1,500$  mV voltage results in a maximum depolarization of  $\sim 35$  mV, which is sufficient to elicit an action potential. Reproduced from [50] © The Author(s)

microelectrode for comparison. Nonetheless, a number of mechanisms could account for the observed changes. These include small alterations in the neurons' resting potential, changes in the junctional membrane resistance, or seal resistance (see Sect. 3.4.5, equivalent electrical circuit of the in-cell configuration). To the best of our knowledge, such recording sessions of intracellular readout with lengths of over 2 days were never conducted prior to this study.

### 3.4.5 In-Cell Configuration: Ohmic Conductance at the gMμE–Neuron Junction

The unprecedented electrical coupling between neurons and engulfed gMμEs can be explained by the use of the analog electrical *equivalent* circuit shown in Fig. 3.11. The model includes the following: (a) a neuron composed of a non-junctional membrane characterized by a passive RC circuit with parameters ( $R_{nj}$ ;  $C_{nj}$ ) and a

junctional membrane facing the gM $\mu$ E ( $R_j$ ;  $C_j$ ), (b) the cleft formed between the neuron's plasma membrane and the surface of the gM $\mu$ E ( $R_{\text{seal}}$ ), and (c) the gM $\mu$ E itself ( $R_{\text{gM}\mu\text{E}}$  and  $C_{\text{gM}\mu\text{E}}$ ). The majority of parameters used for the simulation was obtained from direct measurements or by calculations of the physical parameters that fit the specific geometry of the gM $\mu$ E and the neuron–gM $\mu$ E interface (for further detail, see [50]). The expected coupling coefficient for action potentials (high frequencies of 100–1,000 Hz) and long (DC) pulses were calculated as a function of  $R_{\text{seal}}$  using different values for the junctional membrane resistance (ranging from 10 M $\Omega$  to 100 G $\Omega$ , Fig. 3.11b, c).  $R_{\text{seal}}$  was taken to be  $\sim$ 100 M $\Omega$  (see Sect. 3.3.1 and [48]).

Based on these parameters, we evaluated the range of possible values of the junctional membrane resistance which generate the experimentally observed coupling coefficient (i.e., 0.05–0.5) to be 10–100 M $\Omega$ . Assuming that the junctional membrane conductance is increased by recruitment of voltage-independent ionic channels such as potassium channels with single-channel conductance of 10–100 pS, then  $\sim$ 10–100 such channels have to concentrate within the confined area of the junctional membrane. This would imply a density of approximately 0.5–10 channels/ $\mu\text{m}^2$ . This density is physiological and was documented in many cell types [85].

It is important to recall that the coupling between the neurons and the gM $\mu$ Es depends on the value of  $R_{\text{seal}}$ . Reducing  $R_{\text{seal}}$  to values below 100 M $\Omega$  reduces the coupling coefficient drastically (Fig. 3.11b, c).

Using the same values, it is also possible to simulate the experiments of Fig. 3.9e, modeling the membrane depolarization induced by the delivery of a millisecond long voltage stimulation pulse by a gM $\mu$ E. Figure 3.11d depicts the membrane depolarization induced by such a pulse assuming that  $R_j = 100$  M $\Omega$ ,  $R_{\text{seal}} = 100$  M $\Omega$ , and gM $\mu$ E capacitance is either low (5 pF) or high (40 pF). We have found that for high-capacitance gM $\mu$ Es, an  $\sim$ 1,500 mV voltage results in a maximum depolarization of  $\sim$ 35 mV, which is sufficient to elicit an action potential. This correlates with the empirical findings as shown in Fig. 3.9e.

As discussed in Sect. 3.3, engulfment of gM $\mu$ Es is much more effective when they are functionalized with EPP than with PLL. This suggests that EPP plays a role in the induction of the engulfment and that binding between receptors displayed on the plasma membrane and the EPP activates a highly conserved cascade leading to phagocytosis-like processes [54]. The neurons then elevate the conductance of their plasma membrane facing the gM $\mu$ Es in concert with the assembly of a cytoskeletal actin ring around the stalk of the gM $\mu$ Es. The geometry of the gM $\mu$ Es plays an important role in these cytoskeletal reorganizations [48] as sensing of surface topography by the cell plays a significant role in the regulation of cell functions (for review, see [86]). Convex surfaces are known to cause BAR-domain protein (Bin, Amphiphysin, Rvs domain) to release Rac (a GTPase), which in turn leads to local cytoskeleton rearrangements. This may result in redistribution of ion channels and the introduction of ohmic conductance at the neuron–gM $\mu$ E junction. In addition, changes in mechanical tension of the inner and outer faces of the lipid bilayer by the curvature of the gM $\mu$ E geometry may result in the activation of ion channels or passive increase in local conductance.

### 3.5 Concluding Remarks

We have seen that the neuron–gM $\mu$ Es interface forms an unexpectedly tight junction which supports high-quality bidirectional electrical coupling. This configuration enables in-cell recording with quality and signal-to-noise ratio that matches classical sharp- and patch-electrode intracellular recording. The interface also supports “in-cell stimulation” by milliseconds-long single pulses without damaging the cell membrane. Consistent with the extracellular position of the gM $\mu$ Es with respect to the neurons, the recording sessions could last for over 2 days and most likely for significantly longer periods.

A number of challenges lie in the path toward the translation of in-cell recording and stimulation to in vivo mammalian neural networks [57, 58]. A more sophisticated chemical functionalization of the device, suitable for the diverse population of cell types in the living brain, will most likely be necessary in order to specifically target neurons and prevent professional phagocytotic cells such as microglia from engulfing the electrodes.

**Acknowledgments** The author was supported by a doctoral scholarship from the Israeli Council for Higher Education, a postdoctoral fellowship from the Edmond & Lily Safra Center for Brain Sciences (ELSC), and a fellowship from the European Molecular Biology Organization (EMBO). The research described in this chapter was originated in the laboratory of Prof. Micha E. Spira in collaboration with Prof. Joseph Shappir of the Hebrew University of Jerusalem, Israel.

### References

- Bernstein, J.: Ueber den zeitlichen Verlauf der negativen Schwankung des Nervenstroms. *Pflüger's Arch. ges. Physiol.* **1**, 173–207 (1868)
- Galvani, L.: De viribus electricitatis in motu musculari commentarius. *Bon Sci Art Inst Acad Comm* **7**, 363–418 (1791)
- Galvani, L.: Opere edite ed inedite del Professore Luigi Galvani raccolte e pubblicate dall'Accademia delle Scienze dell'Istituto di Bologna. Dall'Olmo, Bologna (1841)
- Helmholtz, H.: Note sur la vitesse de propagation de l'agent nerveux dans le nerfs rachidiens. *C R Acad Sci (Paris)* **30**, 204–206 (1850)
- Verkhratsky, A., Krishtal, O. A. & Petersen, O. H.: From Galvani to patch clamp: the development of electrophysiology. *Pflügers Arch* **453**, 233–247 (2006)
- Hodgkin, A. L.: Evidence for electrical transmission in nerve: Part II. *J Physiol* **90**, 211–232 (1937)
- Armstrong, C. M.: Life among the axons. *Annu Rev Physiol* **69**, 1–18 (2007)
- Grundfest, H.: The mechanisms of discharge of the electric organs in relation to general and comparative electrophysiology. *Prog Biophys Biophys Chem* **7**, 1–85 (1957)
- Eccles, J. C., Eccles, R. M. & Lundberg, A.: Synaptic actions on motoneurons in relation to the two components of the group I muscle afferent volley. *J Physiol* **136**, 527–546 (1957)
- Hodgkin, A. H., Huxley, A.F.: Action potentials recorded from inside a nerve fibre. *Nature* **144**, 710–711 (1939)
- Sakmann, B. & Neher, E.: Patch clamp techniques for studying ionic channels in excitable membranes. *Annu Rev Physiol* **46**, 455–472 (1984)

12. Berger, T. K., Perin, R., Silberberg, G. & Markram, H.: Frequency-dependent disynaptic inhibition in the pyramidal network: a ubiquitous pathway in the developing rat neocortex. *J Physiol* **587**, 5411–5425 (2009)
13. Hochberg, L. R. et al.: Neuronal ensemble control of prosthetic devices by a human with tetraplegia. *Nature* **442**, 164–171 (2006)
14. Hartline, F. F.: Biological applications for voltage sensitive dyes. *Science* **203**, 992–994 (1979)
15. Loew, L. M., Cohen, L. B., Salzberg, B. M., Obaid, A. L. & Bezanilla, F.: Charge-shift probes of membrane potential. Characterization of aminostyrylpyridinium dyes on the squid giant axon. *Biophys J* **47**, 71–77 (1985)
16. Shoham, D. et al.: Imaging cortical dynamics at high spatial and temporal resolution with novel blue voltage-sensitive dyes. *Neuron* **24**, 791–802 (1999)
17. Stosiek, C., Garaschuk, O., Holthoff, K. & Konnerth, A.: In vivo two-photon calcium imaging of neuronal networks. *Proc Natl Acad Sci U S A* **100**, 7319–7324 (2003)
18. Higley, M. J. & Sabatini, B. L.: Calcium signaling in dendrites and spines: practical and functional considerations. *Neuron* **59**, 902–913 (2008)
19. Rothschild, G., Nelken, I. & Mizrahi, A.: Functional organization and population dynamics in the mouse primary auditory cortex. *Nat Neurosci* **13**, 353–360 (2010)
20. Kwong, K. K. et al.: Dynamic magnetic resonance imaging of human brain activity during primary sensory stimulation. *Proc Natl Acad Sci U S A* **89**, 5675–5679 (1992)
21. Bandettini, P. A., Jesmanowicz, A., Wong, E. C. & Hyde, J. S.: Processing strategies for time-course data sets in functional MRI of the human brain. *Magn Reson Med* **30**, 161–173 (1993)
22. Boyden, E. S., Zhang, F., Bamberg, E., Nagel, G. & Deisseroth, K.: Millisecond-timescale, genetically targeted optical control of neural activity. *Nat Neurosci* **8**, 1263–1268 (2005)
23. Deisseroth, K. et al.: Next-generation optical technologies for illuminating genetically targeted brain circuits. *J Neurosci* **26**, 10380–10386 (2006)
24. Gradinaru, V. et al.: Targeting and readout strategies for fast optical neural control in vitro and in vivo. *J Neurosci* **27**, 14231–14238 (2007)
25. Lee, J. H. et al.: Global and local fMRI signals driven by neurons defined optogenetically by type and wiring. *Nature* **465**, 788–792 (2010)
26. Bradley, P. M., Murphy, D., Kasparov, S., Croker, J. & Paton, J. F.: A micro-optrode for simultaneous extracellular electrical and intracellular optical recording from neurons in an intact oscillatory neuronal network. *J Neurosci Methods* **168**, 383–395 (2008)
27. Zhang, J. et al.: A microelectrode array incorporating an optical waveguide device for stimulation and spatiotemporal electrical recording of neural activity. *Conf Proc IEEE Eng Med Biol Soc* **2009**, 2046–2049 (2009)
28. Anikeeva, P. et al.: Optrode: a multichannel readout for optogenetic control in freely moving mice. *Nat Neurosci* **15**, 163–170 (2012)
29. Logothetis, N. K.: What we can do and what we cannot do with fMRI. *Nature* **453**, 869–878 (2008)
30. Berdondini, L. et al.: Active pixel sensor array for high spatio-temporal resolution electrophysiological recordings from single cell to large scale neuronal networks. *Lab Chip* **9**, 2644–2651 (2009)
31. Bologna, L. L. et al.: Low-frequency stimulation enhances burst activity in cortical cultures during development. *Neuroscience* **165**, 692–704 (2010)
32. Shahaf, G. et al.: Order-based representation in random networks of cortical neurons. *PLoS Comput Biol* **4**, e1000228 (2008)
33. Rubehn, B., Bosman, C., Oostenveld, R., Fries, P. & Stieglitz, T.: A MEMS-based flexible multichannel ECoG-electrode array. *J Neural Eng* **6**, 036003 (2009)
34. Hutzler, M. et al.: High-resolution multitransistor array recording of electrical field potentials in cultured brain slices. *J Neurophysiol* **96**, 1638–1645 (2006)
35. Wise, K. D. & Najafi, K.: Microfabrication techniques for integrated sensors and microsystems. *Science* **254**, 1335–1342 (1991)
36. Campbell, P. K., Jones, K. E., Huber, R. J., Horch, K. W. & Normann, R. A.: A silicon-based, three-dimensional neural interface: manufacturing processes for an intracortical electrode array. *IEEE Trans Biomed Eng* **38**, 758–768 (1991)

37. Shein, M. et al.: Engineered neuronal circuits shaped and interfaced with carbon nanotube microelectrode arrays. *Biomedical Microdevices* **11**, 495–501 (2009)
38. Eytan, D. & Marom, S.: Dynamics and effective topology underlying synchronization in networks of cortical neurons. *J Neurosci* **26**, 8465–8476 (2006)
39. McCreery, D., Pikov, V. & Troyk, P. R.: Neuronal loss due to prolonged controlled-current stimulation with chronically implanted microelectrodes in the cat cerebral cortex. *J Neural Eng* **7**, 036005 (2010)
40. Fromherz, P.: Neuroelectronic Interfacing: Semiconductor Chips with Ion Channels, Nerve Cells and Brain. In: Waser, P. (ed.) *Neuroelectronic interfacing: Semiconductor chips with ion channels, nerve cells, and brain*. Wiley-VCH, Berlin (2003)
41. Fromherz, P., Offenhausser, A., Vetter, T. & Weis, J.: A neuron-silicon junction: a Retzius cell of the leech on an insulated-gate field-effect transistor. *Science* **252**, 1290–1293 (1991)
42. Fromherz, P.: Three levels of neuroelectronic interfacing: silicon chips with ion channels, nerve cells, and brain tissue. *Ann N Y Acad Sci* **1093**, 143–160 (2006)
43. Neves, G., Cooke, S. F. & Bliss, T. V.: Synaptic plasticity, memory and the hippocampus: a neural network approach to causality. *Nat Rev Neurosci* **9**, 65–75 (2008)
44. Spira, M. E. & Hai, A.: Multi-electrode array technologies for neuroscience and cardiology. *Nat Nanotechnol* **8**, 83–94 (2013)
45. Shoham, S., Fellows, M. R. & Normann, R. A.: Robust, automatic spike sorting using mixtures of multivariate t-distributions. *J Neurosci Methods* **127**, 111–122 (2003)
46. Fee, M. S., Mitra, P. P. & Kleinfeld, D.: Automatic sorting of multiple unit neuronal signals in the presence of anisotropic and non-Gaussian variability. *J Neurosci Methods* **69**, 175–188 (1996)
47. Spira, M.E. et al.: Improved neuronal adhesion to the surface of electronic device by engulfment of protruding micro-nails fabricated on the chip surface. *Transducers '07 & Eurosensors Xxi, Digest of Technical Papers, Vols 1 and 2*, 1247–1250 (2007)
48. Hai, A. et al.: Spine-shaped gold protrusions improve the adherence and electrical coupling of neurons with the surface of micro-electronic devices. *J R Soc Interface* **6**, 1153–1165 (2009)
49. Hai, A. et al.: Changing gears from chemical adhesion of cells to flat substrata toward engulfment of micro-protrusions by active mechanisms. *J Neural Eng* **6**, 066009 (2009)
50. Hai, A., Shappir, J. & Spira, M. E.: Long-term, multisite, parallel, in-cell recording and stimulation by an array of extracellular microelectrodes. *J Neurophysiol* **104**, 559–568 (2010)
51. Hai, A., Shappir, J. & Spira, M. E.: In-cell recordings by extracellular microelectrodes. *Nat Methods* **7**, 200–202 (2010)
52. Hai, A. & Spira, M. E.: On-chip electroporation, membrane repair dynamics and transient in-cell recordings by arrays of gold mushroom-shaped microelectrodes. *Lab Chip* **12**, 2865–2873 (2012)
53. Roelandse, M., Welman, A., Wagner, U., Hagmann, J. & Matus, A.: Focal motility determines the geometry of dendritic spines. *Neuroscience* **121**, 39–49 (2003)
54. Stuart, L. M. & Ezekowitz, R. A.: Phagocytosis: elegant complexity. *Immunity* **22**, 539–550 (2005)
55. Dupuy, A. G. & Caron, E.: Integrin-dependent phagocytosis: spreading from microadhesion to new concepts. *J Cell Sci* **121**, 1773–1783 (2008)
56. Geiger, B., Spatz, J. P. & Bershadsky, A. D.: Environmental sensing through focal adhesions. *Nat Rev Mol Cell Biol* **10**, 21–33 (2009)
57. Fendyur, A. & Spira, M. E.: Toward on-chip, in-cell recordings from cultured cardiomyocytes by arrays of gold mushroom-shaped microelectrodes. *Front Neuroeng* **5**, 21 (2012)
58. Fendyur, A., Mazurski, N., Shappir, J. & Spira, M. E.: Formation of Essential Ultrastructural Interface between Cultured Hippocampal Cells and Gold Mushroom-Shaped MEA- Toward “IN-CELL” Recordings from Vertebrate Neurons. *Front Neuroeng* **4**, 14 (2012)
59. Oren, R. et al.: Electrically conductive 2D-PAN-containing surfaces as a culturing substrate for neurons. *J Biomater Sci Polym Ed* **15**, 1355–1374 (2004)
60. Cohen, A., Shappir, J., Yitzchaik, S. & Spira, M. E.: Reversible transition of extracellular field potential recordings to intracellular recordings of action potentials generated by neurons grown on transistors. *Biosens Bioelectron* **23**, 811–819 (2008)

61. Studer, D., Humbel, B. M. & Chiquet, M.: Electron microscopy of high pressure frozen samples: bridging the gap between cellular ultrastructure and atomic resolution. *Histochem Cell Biol* **130**, 877–889 (2008)
62. Castellano, F., Chavrier, P. & Caron, E.: Actin dynamics during phagocytosis. *Semin Immunol* **13**, 347–355 (2001)
63. Sahly, I., Erez, H., Khoutorsky, A., Shapira, E. & Spira, M. E.: Effective expression of the green fluorescent fusion proteins in cultured Aplysia neurons. *J Neurosci Methods* **126**, 111–117 (2003)
64. Sahly, I., Khoutorsky, A., Erez, H., Prager-Khoutorsky, M. & Spira, M. E.: On-line confocal imaging of the events leading to structural dedifferentiation of an axonal segment into a growth cone after axotomy. *J Comp Neurol* **494**, 705–720 (2006)
65. Decourt, B., Munnamalai, V., Lee, A. C., Sanchez, L. & Suter, D. M.: Cortactin Colocalizes With Filopodial Actin and Accumulates at IgCAM Adhesion Sites in Aplysia Growth Cones. *Journal of Neuroscience Research* **87**, 1057–1068 (2009)
66. Endlich, N., Otey, C. A., Kriz, W. & Endlich, K.: Movement of stress fibers away from focal adhesions identifies focal adhesions as sites of stress fiber assembly in stationary cells. *Cell Motil Cytoskeleton* **64**, 966–76 (2007)
67. Bradke, F., Fawcett, J. W. & Spira, M. E.: Assembly of a new growth cone after axotomy: the precursor to axon regeneration. *Nat Rev Neurosci* **13**, 183–193 (2012)
68. Pollard, T. D. & Cooper, J. A.: Actin and actin-binding proteins. A critical evaluation of mechanisms and functions. *Annu Rev Biochem* **55**, 987–1035 (1986)
69. Bailey, C. H. & Chen, M.: Time course of structural changes at identified sensory neuron synapses during long-term sensitization in Aplysia. *J Neurosci* **9**, 1774–1780 (1989)
70. Honkura, N., Matsuzaki, M., Noguchi, J., Ellis-Davies, G. C. & Kasai, H.: The subspine organization of actin fibers regulates the structure and plasticity of dendritic spines. *Neuron* **57**, 719–729 (2008)
71. Bourne, J., Morgan, J. R. & Pieribone, V. A.: Actin polymerization regulates clathrin coat maturation during early stages of synaptic vesicle recycling at lamprey synapses. *J Comp Neurol* **497**, 600–609 (2006)
72. Shupliakov, O. et al.: Impaired recycling of synaptic vesicles after acute perturbation of the presynaptic actin cytoskeleton. *Proc Natl Acad Sci U S A* **99**, 14476–14481 (2002)
73. Malkinson, G. et al.: Calcium-induced exocytosis from actomyosin-driven, motile varicosities formed by dynamic clusters of organelles. *Brain Cell Biol* **35**, 57–73 (2006)
74. Benbassat, D. & Spira, M. E.: The Survival of Transected Axonal Segments of Cultured Aplysia Neurons Is Prolonged by Contact with Intact Nerve-Cells. *European Journal of Neuroscience* **6**, 1605–1614 (1994)
75. Mortari, A., Maaroo, A., Martin, D. & Cortie, M. B.: Mesoporous gold electrodes for sensors based on electrochemical double layer capacitance. *Sensors and Actuators B-Chemical* **123**, 262–268 (2007)
76. McGillivray, R. & Wald, R.: Dual-path capacitance compensation network for microelectrode recordings. *Am J Physiol* **238**, H930–1 (1980)
77. Wilson, C. J. & Park, M. R.: Capacitance compensation and bridge balance adjustment in intracellular recording from dendritic neurons. *J Neurosci Methods* **27**, 51–75 (1989)
78. Schoen, I. & Fromherz, P.: Extracellular stimulation of mammalian neurons through repetitive activation of Na<sup>+</sup> channels by weak capacitive currents on a silicon chip. *Journal of Neurophysiology* **100**, 346–357 (2008)
79. Ryttsen, F. et al.: Characterization of single-cell electroporation by using patch-clamp and fluorescence microscopy. *Biophys J* **79**, 1993–2001 (2000)
80. Rubinsky, B.: Irreversible electroporation in medicine. *Technol Cancer Res Treat* **6**, 255–260 (2007)
81. Brummer, S. B., Robblee, L. S. & Hambrecht, F. T.: Criteria for selecting electrodes for electrical stimulation: theoretical and practical considerations. *Ann N Y Acad Sci* **405**, 159–171 (1983)
82. Harnack, D. et al.: The effects of electrode material, charge density and stimulation duration on the safety of high-frequency stimulation of the subthalamic nucleus in rats. *J Neurosci Methods* **138**, 207–216 (2004)

83. Yao, Y. et al.: Influence of electroporation on the biological activities of primary rat hepatocytes. *Zhonghua Gan Zang Bing Za Zhi* **9**, 178–180 (2001)
84. Merrill, D. R., Bikson, M. & Jefferys, J. G.: Electrical stimulation of excitable tissue: design of efficacious and safe protocols. *J Neurosci Methods* **141**, 171–198 (2005)
85. Hille, B.: *Ion Channels of Excitable Membranes*. Sinauer, Sunderland, MA (2001)
86. Vogel, V. & Sheetz, M.: Local force and geometry sensing regulate cell functions. *Nat Rev Mol Cell Biol* **7**, 265–275 (2006)